

AD-A102 283

ITEK CORP. LEXINGTON MASS OPTICAL SYSTEMS DIV  
SOLAR IMAGING EXPERIMENT.(U)  
SEP 80 J W HARDY

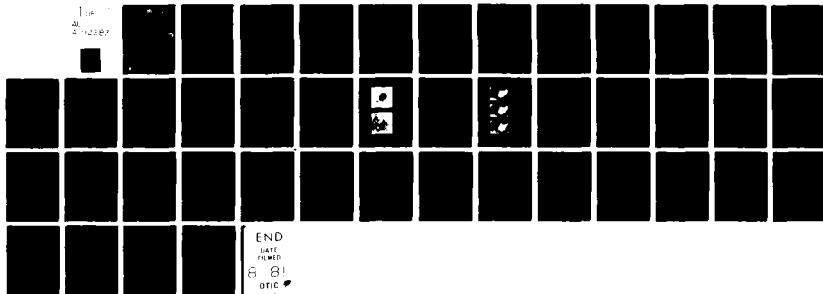
F/6 3/1

UNCLASSIFIED

AFGL-TR-80-0338

F19628-79-C-0077  
NL

11a  
4  
242260



**LEVEL**

12  
BS

AFGL-TR-80-0338 ✓

AD A102283

SOLAR IMAGING EXPERIMENT

John W. Hardy

Itek Corporation  
Optical Systems Division  
10 Maguire Road  
Lexington, Massachusetts 02173

Final Report  
February 1979-June 1980

DTIC  
ELECTED  
AUG 3 1981  
C

September 1980

Approved for public release; distribution unlimited

This research was supported by the Air Force In-House  
Laboratory Independent Research Fund

AIR FORCE GEOPHYSICS LABORATORY  
AIR FORCE SYSTEMS COMMAND  
UNITED STATES AIR FORCE  
HANSCOM AFB, MASSACHUSETTS 01731

FILE COPY

81 7 31 082

**Qualified requestors may obtain additional copies from the  
Defense Technical Information Center. All others should  
apply to the National Technical Information Service.**



Unclassified

SECURITY CLASSIFICATION OF THIS PAGE(When Data Entered)

20 - continued

second period, observations were also made of single and double stars to obtain data on the isoplanatic patch. The compensated image was recorded on videotape using an ISIT camera. In addition, 48 channels of real-time RTAC data (including deformable mirror drive signals) were digitized and recorded on 9-track tape.

With stars, the real-time compensation system operated as expected, sharpening the image and producing a significant increase in peak intensity. Observations of double stars indicated that the isoplanatic patch radius at night was between 2 and 4 arcseconds near the zenith.

When observing the sun, it was found that the image stabilization system worked efficiently even with bad turbulence. However, the expected improvement in image sharpness due to the deformable mirror was obtained only on some occasions and could not generally be predicted, in spite of the fact that the RTAC appeared to operate normally with all feedback loops closed and small residual errors.

These results appear to be due to atmospheric parameters, primarily the small size of the isoplanatic patch and the small values of turbulence coherence length during the day.

These two factors reduce both the compensated field size and the compensated aperture size (for a fixed number of actuators) resulting in a small number of compensated image elements.

This experiment has confirmed the feasibility of real-time compensation of solar images. However, much work remains to be done to refine the technique. Further operational systems should employ larger apertures (necessitating a much larger number of actuators) in order to maximize the number of resolved image elements within the compensated field.

Unclassified

SECURITY CLASSIFICATION OF THIS PAGE(When Data Entered)

SOLAR IMAGING EXPERIMENT

List of Contributing Scientists and Engineers:

J. W. Hardy  
J. E. Lefebvre  
S. R. Moody  
J. T. Smith  
E. P. Wallner  
R. V. Wientzen

Accession For	
NTIS GPA&I	<input checked="" type="checkbox"/>
DTIC TAB	<input type="checkbox"/>
Unannounced	<input type="checkbox"/>
Justification	
By _____	
Distribution/	
Availability Codes	
Avail and/or	
Dist	Special
A	

## CONTENTS

	Page
1. OBJECTIVES . . . . .	1
2. EQUIPMENT . . . . .	3
3. OBSERVATIONS	
3.1 First Observing Period . . . . .	11
3.1.1 Stellar Images . . . . .	11
3.1.2 Solar Images . . . . .	11
3.2 Second Observing Period	
3.2.1 Solar Images . . . . .	13
3.2.2 Stellar Images . . . . .	13
3.3 Data Summary . . . . .	15
4. ANALYSIS	
4.1 Coherence Length . . . . .	28
4.2 Isoplanatic Patch . . . . .	30
5. CONCLUSIONS . . . . .	36

## FIGURES

	Page
1. Solar Telescope Image Compensation System . . . . .	4
2. Video Image Scale Factors . . . . .	5
3. Actuator and Detector Locations . . . . .	9
4. Real-Time Compensation of Star Arcturus . . . . .	12
5. Real-Time Compensation of Sunspot . . . . .	14
6. Intensity Profiles of Arcturus . . . . .	16
7. Intensity Profiles of Castor . . . . .	17
8. Intensity Profiles of Algieba . . . . .	18
9. Real-Time Data Print-out . . . . .	22
10. Power Spectrum of Actuator Drive Signal . . . . .	23
11. Spatial Correlation, Night Observations . . . . .	25
12. Intensity Correlation, Night Observations . . . . .	26
13. Diurnal Variation of Turbulence Coherence Length . . . . .	29
14. Variation of Effective Solar Coherence Length . . . . .	29
15. Wavefront Error Due to Anisoplanation . . . . .	32
16. Image Quality versus Field Angle . . . . .	33
17. Diurnal Variation of Solar Compensated Field . . . . .	34

## 1. OBJECTIVES

The prime objective of this program is to make an experimental investigation of the feasibility of real-time compensation of the solar photosphere, with the goal of obtaining high-resolution images showing the structure and evolution of the solar granulation pattern. Such data are of great potential value in advancing our understanding of the physical processes taking place in the sun. An important practical consequence will be an improvement in our capability of predicting magnetic storms and radiation outbursts that have a considerable effect on military communications and sensing systems.

The best currently available images of solar granulation obtained with ground-based telescopes are limited by atmospheric turbulence to a resolution of 1 to 2 arc-sec with occasional frames showing sub-arc-sec detail. Speckle interferometric measurements made with the 76-cm Vacuum Tower Telescope at Sacramento Peak Observatory indicate the presence of detail in the solar granulation up to at least 2.5 cycles/arc-sec. An initial goal was therefore to demonstrate consistent imaging of 0.4 arc-sec solar detail, a goal that should be achievable using a modified version of Itek's 21-channel Real-Time Atmospheric Compensation (RTAC) system.

The RTAC employs a deformable mirror with 21 independent actuators, driven in the closed-loop mode by a wavefront sensor which operates with white-light reference sources. The response time of the RTAC feedback loop is about 1 millisecond, which is fast enough to compensate atmospheric turbulence in ground-based telescopes. For the normal range of atmospheric turbulence strength at good sites ( $r_0 = 6$  to 12 cm), the RTAC is capable of compensating telescope apertures of 30 to 60 cm. A full description of the RTAC is given in the Reference 1.

The RTAC was originally designed to operate with near-point reference sources, such as stars and other small-diameter astronomical objects. Recent laboratory experiments have shown the feasibility of modifying the wavefront sensor so that very bright objects (such as the sun) containing detail in the sub-arc-second range can be used as the source. The present experiment is therefore planned to validate this application of the RTAC using small sections of the solar disk as the wavefront reference.

If successful, the experiment should yield improved solar images over extended times of several hours. It should also allow the use of high spatial resolution spectroscopy by isolating sections of the solar granulation that are normally blurred by atmospheric seeing.

The impact of this technique on the future of ground-based solar observations is considerable, as it will give a new lease of life to the many existing solar observatories, and allow the collection of high resolution data otherwise obtainable only from space.

The secondary objective of the program is to obtain measurements of the size of the isoplanatic patch by observing binary stars of varying separations. To perform this test, the RTAC wavefront sensor is modified by the addition of a field stop to isolate the light from one star of the pair, so that the wavefront measurement and resulting compensation are valid for only one line of sight. By recording the images of both stars, and determining the image quality of the second star as a function of the angular separation, the size of the isoplanatic patch can be measured.

In addition to the compensated images recorded on videotape, a considerable data base of real-time outputs from the RTAC, such as deformable mirror drive signals, will also be obtained.

## 2. EQUIPMENT

The Real-Time Atmospheric Compensation (RTAC) system modified for solar operation was installed on a 12-foot optical bench on the operating platform of the 76-cm Vacuum Tower Telescope at Sacramento Peak Observatory in June 1979. A schematic of the system is shown in Figure 1. The prime solar image, which is approximately 0.5 meter in diameter, was focused via the exit port and fold mirror at the end of the optical bench. Most of the sunlight was excluded by a field stop at this point, only a small area of about 20 x 20 arcseconds being used at any one time. The area viewed was selected by driving the turret mirrors in the normal manner. The light from the selected image area was collimated to form a beam exactly 1.00 inch (25.4 mm) in diameter, which was then reflected from the tip-tilt (guider) and deformable mirrors in the RTAC. An optical zoom system on the bench varied the effective focal length of the collimator to allow compensation of primary apertures between 30 and 60 cm. The deformable mirror had five actuators across its diameter so that the effective actuator spacing could be varied in this way from 6 cm to 12 cm to allow for difference atmospheric turbulence coherence lengths.

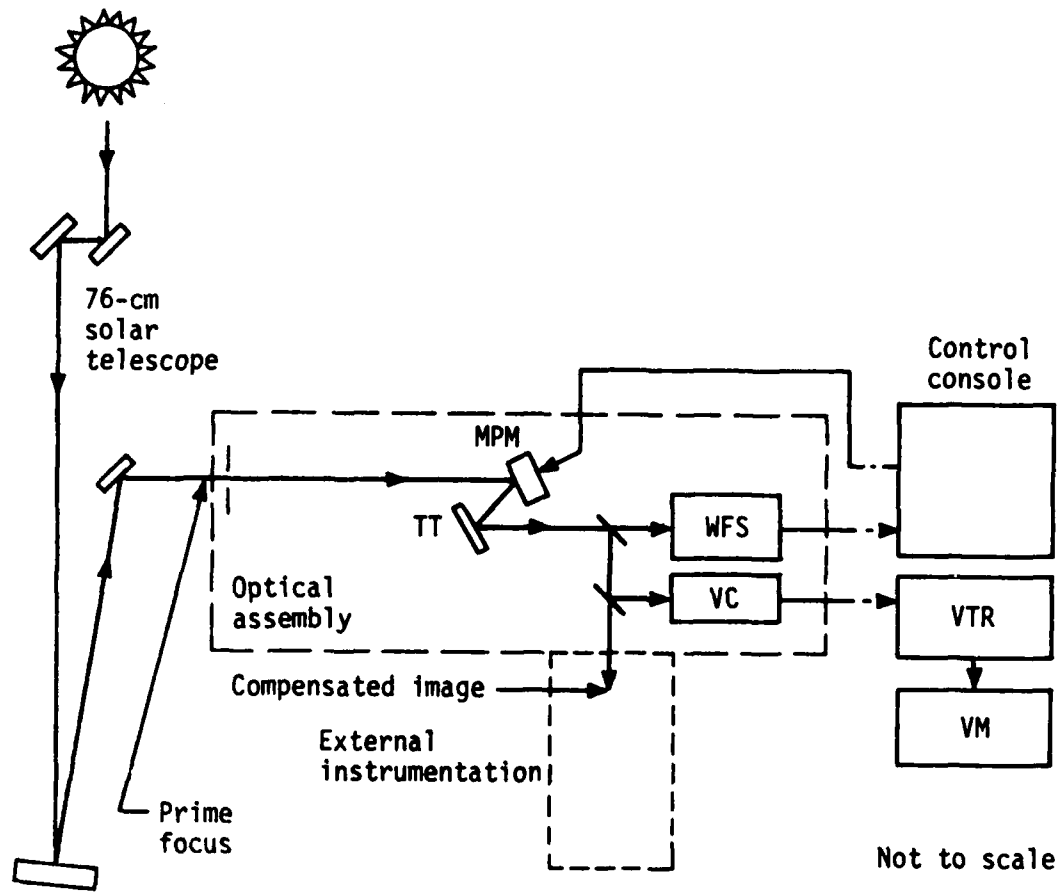
The RTAC system was modified for solar operation by placing a field stop in the wavefront sensor to define small areas of the solar surface, adjustable from about 2 to 8 arcseconds across, for use as the wavefront reference source. The wavefront sensor could be adjusted to lock on to either a bright object in a dark field or a dark object in a bright field.

The deformable mirror employed in the RTAC was a monolithic piezoelectric mirror (MPM) with 21 independently controlled zones. The bandwidth of the servo control loops could be set at 50, 200 or 400 Hz. The two-axis tip-tilt mirror used for overall tilt (or image motion) removal had a bandwidth of 150 Hz.

To provide a real-time indication of RTAC system performance, the residual error signals in all 21 control loops were squared and summed to form a composite overall error voltage that was displayed on a meter.

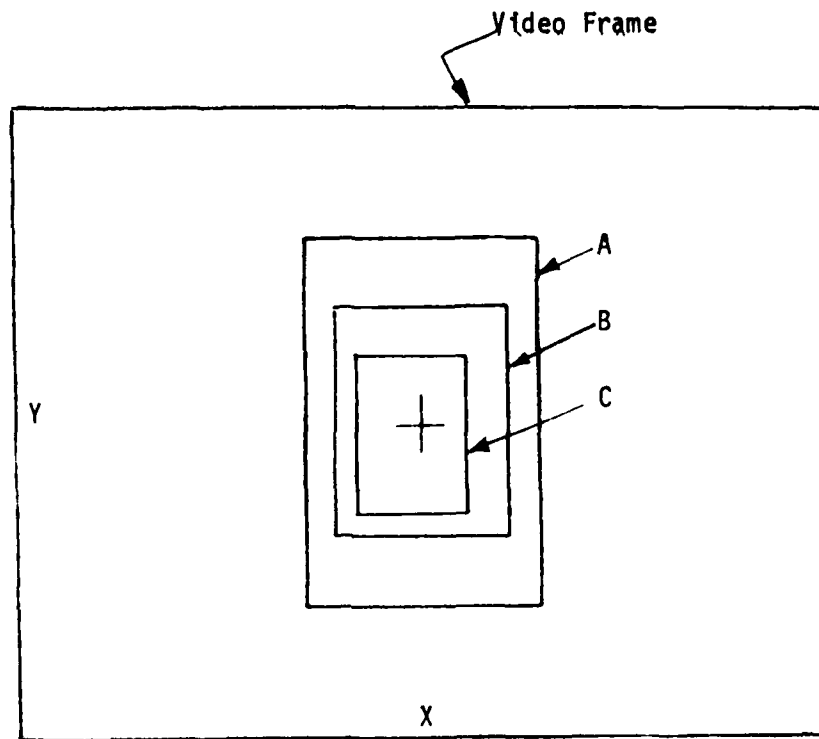
The imaging system consisted of a 525-line TV camera with relay optics to give a field-of-view of 18 x 14 arcseconds at 0.3 meter telescope aperture, or 9 x 7.6 arcseconds at 0.6 meter aperture. Composite video signals were recorded on analog videotape using a video cassette recorder. The video image format and scale factors for the range of field stops used is shown in Figure 2.

A real-time digital data recording system was attached to the RTAC to allow up to 48 channels of data at 1 KHz sampling rate to be recorded on 9-track digital tape. Approximately four minutes of continuous observation could be stored on each 2400 foot tape. The signals recorded are listed in Table 1 and included the drive signals for the tip-tilt mirror and MPM actuators, residual wavefront error, and wavefront sensor light intensities.



- MPM - Monolithic piezoelectric mirror
- TT - Tip-tilt corrector
- WFS - Wavefront sensor
- VC - Video camera
- VM - Video monitor

Fig. 1 Solar telescope image compensation system



VIDEO IMAGE	ANGULAR SIZE			
	D = 0.3m		D = 0.6m	
	X	Y	X	Y
	arc seconds		arc seconds	
Full Frame	18	14	9.0	7.0
Field Stop A	5.3	8.2	2.6	4.1
Field Stop B	3.8	5.5	1.9	2.7
Field Stop C	2.3	3.6	1.1	1.8

Fig. 2 Video Image Scale Factors

TABLE 1  
RTAC DATA CHANNEL ALLOCATION

<u>Channel Number</u>	<u>Description</u>	<u>Signal</u>
1	Tip/tilt loop status	0v-on, +5v-off
2	MPM loop status	0v-on, +5v-off
3	X-tilt drive	±10v
4	Y-tilt drive	±10v
5	Command-start to record data	
6	MPM drive node no. 5	±10v
7	MPM drive node no. 6	±10v
8	MPM drive node no. 7	±10v
9	MPM drive node no. 8	±10v
10	MPM drive node no. 9	±10v
11	MPM drive node no. 10	±10v
12	MPM drive node no. 11	±10v
13	MPM drive node no. 12	±10v
14	MPM drive node no. 13	±10v
15	Seeing monitor output	0-10 volts
16	Residual error output	0-7 volts
17	MPM drive node no. 14	±10v
18	MPM drive node no. 15	±10v
19	MPM drive node no. 16	±10v
20	MPM drive node no. 17	±10v
21	MPM drive node no. 18	±10v
22	MPM drive node no. 19	±10v
23	MPM drive node no. 20	±10v

TABLE 1 (Continued)

<u>Chanel Number</u>	<u>Description</u>	<u>Signal</u>
24	MPM drive node no. 21	10v
25	MPM drive node no. 1	10v
26	MPM drive node no. 2	10v
27	MPM drive node no. 3	10v
28	MPM drive node no. 4	10v
29	Command - use RTAC tracking signals +5, 0.	
30	X-tilt phase error	
31	Y-tilt phase error	
32	Light intensity, PMT	X1
33	Light intensity, PMT	X2
34	Light intensity, PMT	X3
35	Light intensity, PMT	X4
36	Light intensity, PMT	X5
37	Light intensity, PMT	X6
38	Light intensity, PMT	X7
39	Light intensity, PMT	X8
40	Light intensity, PMT	X9
41	Light intensity, PMT	X10
42	Light intensity, PMT	X11
43	Light intensity, PMT	X12
44	Light intensity, PMT	X13
45	Light intensity, PMT	X14
46	Light intensity, PMT	X15
47	Light intensity, PMT	X16
48	Phase error, X4 Phase detector output	

The relation of the deformable mirror actuator zones to the detector locations in the RTAC is shown in Figure 3.

The scale factors for the analog and digital outputs are listed in Table 2.

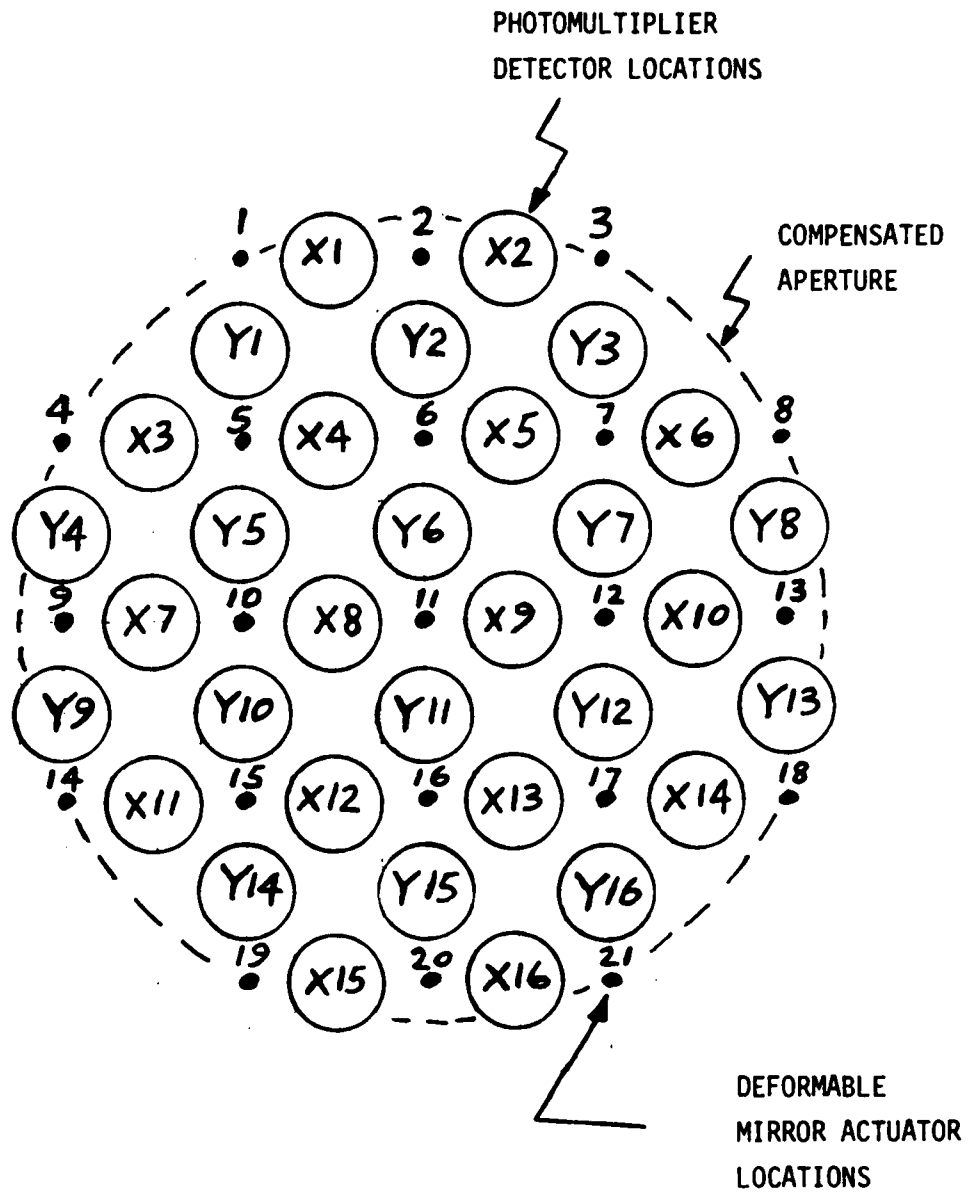


FIGURE 3. ACTUATOR AND DETECTOR LOCATIONS

TABLE 2

## RTAC DATA TAPE CALIBRATION

SIGNAL	ANALOG SCALE FACTOR	RANGE	A/D BITS	DIGITAL SCALE FACTOR
X-Tilt	1.3V/arcsec	±10v	14	2130 per arc sec
Y-Tilt	2.4V/arcsec	±10v	14	3932 per arc sec
MPM (Wavefront)	0.125 μM per volt	±10v	14	13,107 per μM (Wavefront)

### 3. OBSERVATIONS

Observations were made using the RTAC with the 76-cm Vacuum Tower Telescope at Sacramento Peak National Observatory during two periods, 18 through 28 June 1979 and 21 March through 7 April 1980. The telescope time that was allocated enabled observations of the sun during the day and bright stars at night.

#### 3.1 First Observing Period

##### 3.1.1 Stellar Images

It was found that the RTAC produced a significant improvement in stellar images, stabilizing the motion of the seeing disk and reducing its size in many cases to close to the diffraction limit of the telescope (0.2 arc seconds). Compensated and uncompensated images of the Star Arcturus are shown in Figure 4.

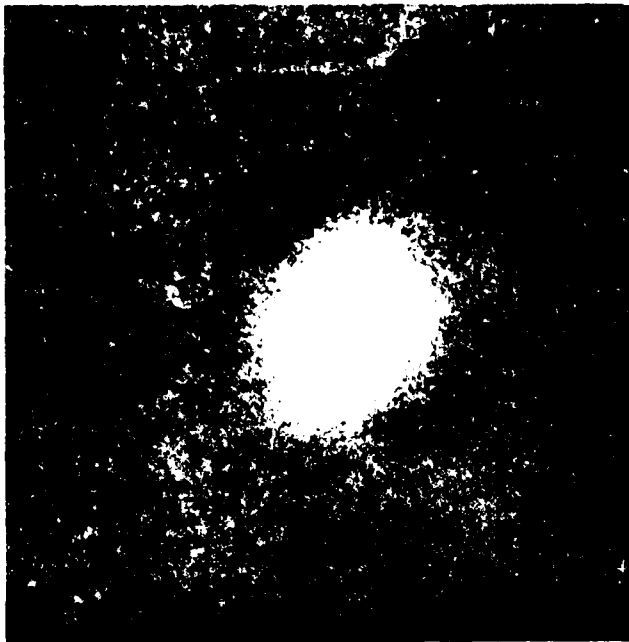
##### 3.1.2 Solar Images

When operating on the sun, the objects used as reference sources were pores and small sunspots a few arcseconds in diameter. Attempts to lock the RTAC on to the solar granulation were not successful.

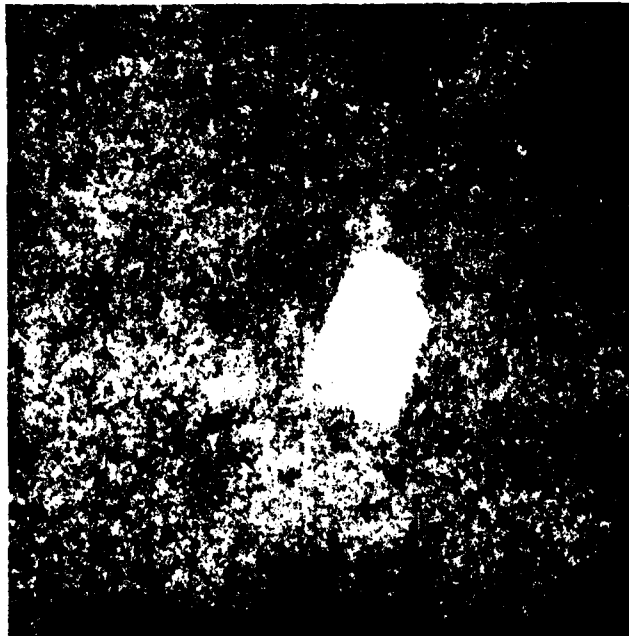
The RTAC achieved image-motion stabilization using the tip-tilt mirror without any difficulty on almost all occasions, even in bad turbulence. When compensating image motion, the reference object in the center of the field of view was well stabilized, but residual image motion due to isoplanatism was usually observed, increasing as a function of radius from the center.

The result of operating the deformable mirror on solar images was somewhat ambiguous. Again, it was possible to close the servo loops (21 in all, one to each actuator of the deformable mirror) on most occasions, even in bad turbulence. The residual wavefront error, as indicated by the phase error variance at the output of the wavefront sensor, was usually reduced to almost zero, showing that the RTAC was in fact efficiently compensating the wavefront errors being measured. However, a noticeable improvement in the resolution of the optical image was apparent only on rare occasions. The most likely reason for the lack of improvement in image detail was that the isoplanatic patch (the image area over which the wavefront error due to atmospheric turbulence is correlated) was much smaller than the actual field of view of the wavefront sensor, resulting in an averaging of the measured wavefront error. Under these conditions, the "measured" wavefront error did not represent the "true" wavefront error in any part of the field of view so that compensation was not effective.

Analysis of anisoplanatic effects has shown that with normal daytime turbulence, the isoplanatic patch near the zenith may only be 1 to 2 arc seconds in radius, rapidly decreasing as the eighth fifths power of the cosine of the zenith angle.



(a) No compensation, ~3 arc-sec seeing



(b) Full wavefront compensation, full-width half-maximum of Airy disk estimated to be 0.25 arc-sec

Fig. 4 — Real-time compensation of Arcturus using 21-actuator deformable mirror (60-cm telescope aperture, 10-sec exposure)

This small isoplanatic angle produces two practical difficulties:

1) If the wavefront sensor field of view is larger than the isoplanatic patch, the degree of improvement possible in image quality is very limited.

2) Even if image compensation is achieved, it will be effective over a very small area. With a small aperture telescope such as the 30 cm compensated aperture achieved with the RTAC, the compensated area includes only a small number of resolution elements.

### 3.2 Second Observing Period

#### 3.2.1 Solar Images

The RTAC wavefront sensor as configured for the June 1979 tests was capable of using areas of the solar surface of  $15 \times 15$  arc seconds down to  $5 \times 5$  arc seconds as the reference source.

To improve performance with small isoplanatic patches, the RTAC was reconfigured at Itek in late 1979 to reduce the wavefront sensor field of view to about  $2 \times 2$  arc seconds. A second series of tests was conducted using the 76 cm Vacuum Tower Telescope at Sacramento Peak between 21 March and 7 April 1980.

This modification was partly successful in that a noticeable improvement in solar image quality was obtained on two occasions, one example being shown in Figure 5. The daytime seeing during this period varied from poor to moderate and it was necessary to use a small telescope aperture (0.3 m). Because of this, the smallest field stop size usable was  $2.3 \times 3.6$  arc seconds. It was again found that on most occasions the RTAC servo loop could be closed, reducing the indicated electrical error signals to near zero. A corresponding improvement in image quality was seen only occasionally, and could not be predicted.

#### 3.2.2 Stellar Images

An objective of the second series of tests was to obtain isoplanatic data from double stars by using one star as the reference and measuring the image quality of the second star as a function of the angular separation.

To facilitate the star tests, it was intended to connect the RTAC tip/tilt outputs to the tracking system of the 76-cm Tower Telescope, which normally cannot track stars accurately. However, this arrangement was not successful due to problems in one of the telescope synchros which could not be fixed in time. We therefore reverted to using the old quad PMT star tracker, which only operates when the sky is completely dark.



(a) No compensation



(b) Tip-tilt (image motion) compensation only



(c) Full wavefront compensation

Fig. 5 — Real-time compensation of sunspot using 21-actuator deformable mirror (30-cm telescope aperture,  $18 \times 13$ -arc-sec field of view, 1/15-sec exposure)

We also found that the RTAC would not lock on with 3rd Magnitude stars due to the optical transmission of the telescope being less than anticipated. These two factors ruled out observation of double stars from night into daylight, because the morning stars were all 3rd magnitude. Consequently, our observations of double stars were restricted to those of 2nd magnitude visible at night, which were:

$\alpha$ UMa	, 1 arc second separation,	Magnitudes	1.88, 4.82
$\alpha$ Gem	, 2.2 arc second separation,	"	2.0, 2.8
$\zeta$ Ori	, 3 " " "	"	1.91, 4.04
$\gamma$ Leo	, 4.3 " " "	"	1.1, 3.4

Images of several single bright stars such as Sirius, Arcturus, and Vega were recorded in addition to the double stars. The improvement in image quality, when the MPM was switched on, was considerable, as shown in the intensity profiles of Figure 6. These profiles are based on the integration of 16 video frames, equivalent to about 1/4 second exposure time.

The double star images were obtained with the RTAC operating near its photon limit. Consequently, the signal to noise ratio is low and the compensation not as effective as with brighter stars. Intensity profiles of  $\alpha$  Gem (Castor) and  $\gamma$  Leo (Algieba) are shown in Figures 7 and 8. In the case of Castor, both star images appear to be equally changed by operation of the MPM, indicating that the isoplanatic patch exceeds 2 arc seconds. The profiles of Algieba clearly show sharpening of the brighter star (used as reference) with degradation of the comparisons indicating that in this instance, the isoplanatic patch is less than 4 arc seconds in radius.

### 3.3 Data Summary

An important output of the Solar Imaging Experiment is the large data base that was collected by recording the real-time signal outputs of the RTAC when observing both during the day and at night. These data are summarized in Table 3, which lists both the videotape cassette and counter numbers, and also the corresponding digital data tape sections.

## INTENSITY PROFILES OF ARCTURUS

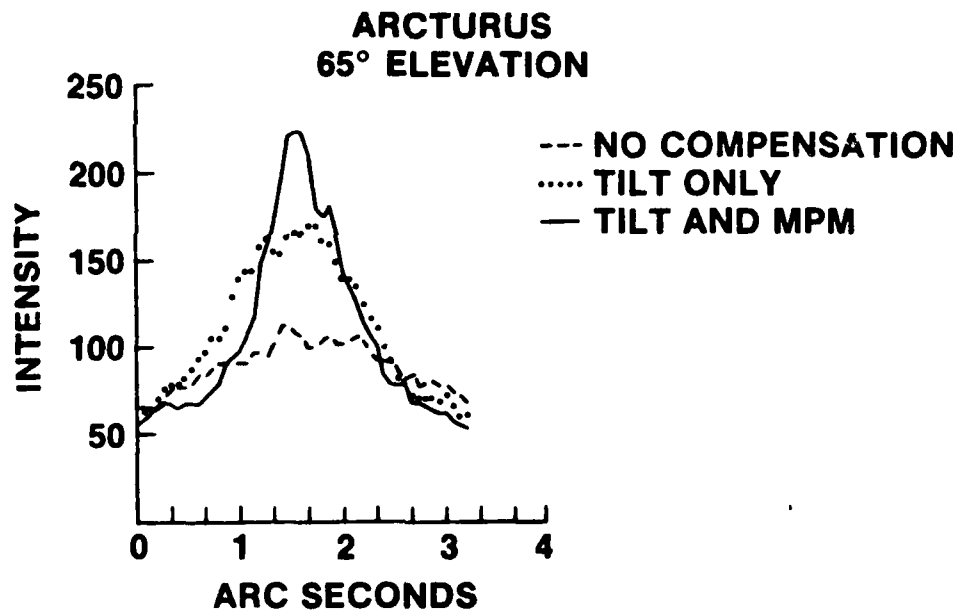


Figure 6. Intensity Profiles of Arcturus

## INTENSITY PROFILES OF CASTOR

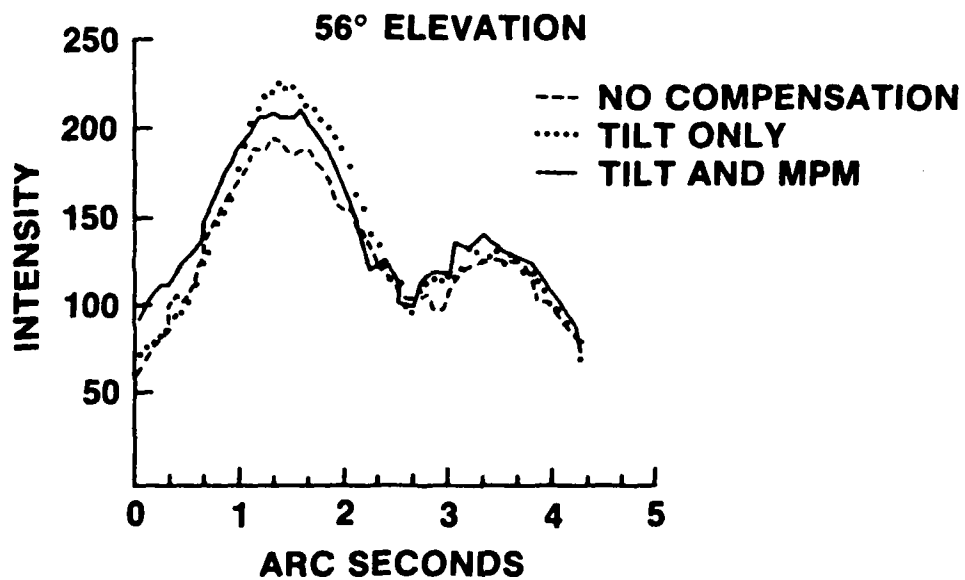


Figure 7. Intensity Profiles of Castor

## INTENSITY PROFILES OF ALGIEBA

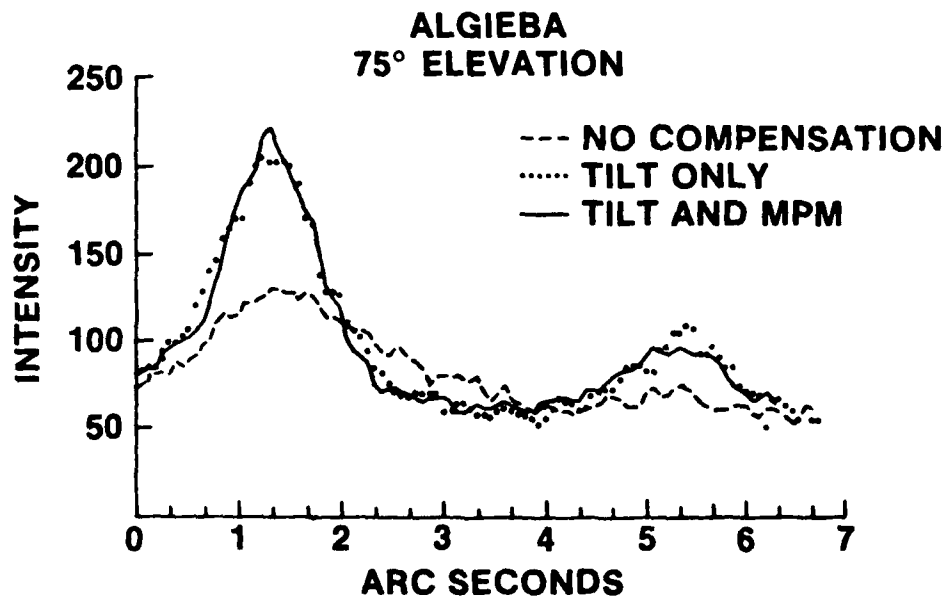


Figure 8. Intensity Profiles of Algieba

TABLE 3  
SAC PEAK OBSERVATIONS MAR/APR 1980

DATA SUMMARY

OBJECT	DATE/TIME HRS.		VIDEOTAPE		DATA TAPE #	REMARKS
			#	INDEX		
Sunspot	3/28	10:00	2	56-84	2	60-75 Best Sunspot images
Sunspot	3/28	11:30	2	120-140	3	Best turbulence
Sunspot	3/29	16:15	2	145-166	4	Best turbulence
Sirius	3/30	20:00	2	183-188	5	
Castor	3/30	22:30	2	188-218	5	Tilt only
Algieba	3/30	25:00	2	234-280	5	Tilt only Vibration (Wind)
Sirius	3/31	21:30	3	000-015	6	0.3M Aperture MPM only
"	3/31	21:30	3	-	6	0.4M " " "
"	3/31	21:30	3	-	6	0.5M " " "
"	3/31	21:30	3	-	6	0.6M " " "
"	3/31	21:30	3	-	6	0.6M Tilt only
"	3/31	21:30	3	-	6	0.6M Tilt & MPM
Sunspot	4/03	11:30	3	032-097	-	Small MPM Improvement
"	4/94	07:30	3	097-117	-	Tilt Anisoplanatism can be seen
"	4/04	09:30	3	125-134	7	
"	4/04	11:00	3	141-153	7	Discard last section of #7 after this
"	4/05	09:30	3	200-210	-	
Arcturus	4/06	02:45	4	032-050	8	Solid
"	4/06	03:00	4	050-080	-	Best 074-077
Sirius	4/06	19:45	4	083-125	9 0 to 1 min10	Some elongation due to dispersion
"	4/06	20:00	4	135-148	-	Demonstration of Disp. Correction
Zeta ORI	4/06	21:00	4	207-220	9 1 min 10 to 3 min40	Poor seeing
Castor	4/06	21:30	4	244-260	9 3 min 40 to 6min 40	
Algieba	4/06	22:30	4	320-330	-	Best comp of Algieba
$\alpha$ UMa	4/06	23:00	4	353-368	-	Best section on $\alpha$ UMa

TABLE 3 - (Continued)

OBJECT	DATE/TIME HRS.	VIDEOTAPE		DATA TAPE #	REMARKS
		#	INDEX		
Arcturus	4/06 23:45	5	015-031	-	015-020 Good 031
Filament Lamp	4/07 18:30	-	-	10	No turbulence, RTAC Baseline
Zeta Orionis	4/07 19:45	5	090-119	-	Best sections 90-91, 95 113-114, 117-119 (BW1)
" "	4/07 19:50	5	120-133	10	
Castor	4/07 21:00	5	202-250	-	Best 224-226 56° EL 236-250
"	4/07 21:20	5	250-265	10	
Algieba	4/07 21:45	5	317-328		BW1 - Best AGC OFF
"	4/07 22:00	5	328-352		BW2 - Not as good
"	4/07 22:30	-	-	10	
Castor	4/07 23:15	6	205-214	-	210-212 OK 30° Elev
"	4/07 23:30	6	231-250	11	
Vega	4/07 23:40	6	250-266	11	20° Elev

END OF OBSERVATIONS

Software to process these data tapes has been generated on the contract. The specific programs developed are:

- a) Summary plot of 4 channels of data from the entire data tape, with Universal time scale.
- b) Power Spectrum computation and plot for designated 2-second periods of any channel.

The following specific items have been delivered under the contract:

1. Documentation of the Power Spectrum Software.
2. Sample test run producing both universal time plots and power spectrum plots.
3. Source code for Power Spectrum Software excluding the FILENO, FOURT, and READIN routines. Both FILENO and FOURT may be obtained from the SHARE Fortran Project and READIN was developed by ITEK and cannot be distributed.
4. Documentation for FILENO, FOURT, and READIN.
5. Magnetic Tape containing source code for Power Spectrum.
6. Magnetic Tape containing power spectrum data.

Examples of the data recorded are shown in Figure 9 and a typical Power Spectrum plot is shown in Figure 10.

Results of the data analysis performed to date are shown in Table 4, Figure 11 and Figure 12. Table 4 lists the temporal bandwidth of the drive signals for tip-tilt and MPM for both daylight and nighttime conditions, together with the root mean square values of the drive signals. Also listed is a single measurement of the bandwidth of the intensity (scintillation) signal for a star (Sirius) at night.

The tip tilt data show little difference between day and night operation, the bandwidth measured at 10% power ranging from about 10 to 40 Hz.

A much greater difference is seen in the MPM drive signal power spectra between day and night operation, the daytime 10% power bandwidth ranging from 60 to 120 Hz, while at night it lies between 20 and 55 Hz. The bandwidth is of course, highly dependent on wind velocity.

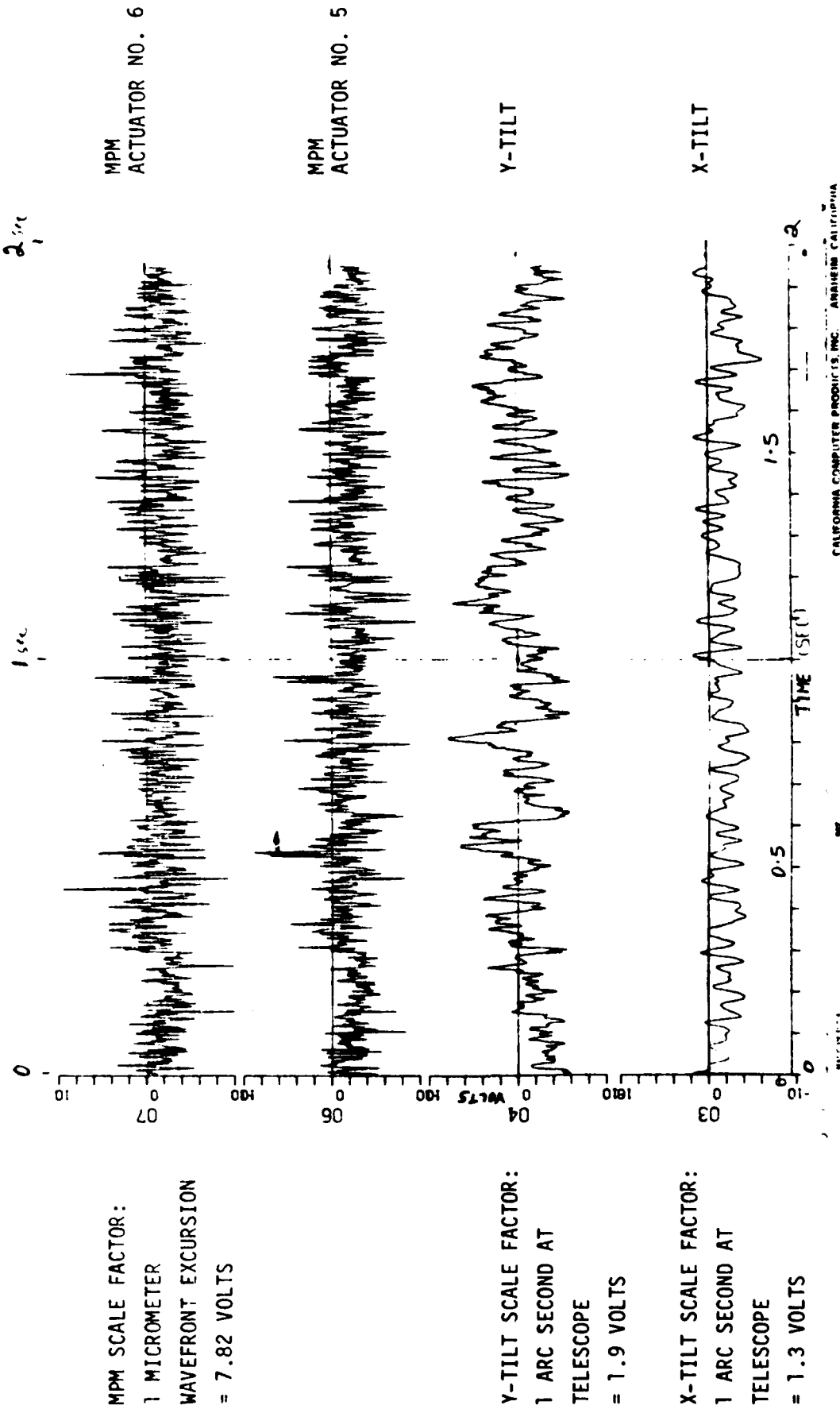


FIGURE 9 REAL-TIME DATA PRINT-OUT, CLOSED-LOOP OPERATION.  
ITEK DATA TAPE NO. 3A, SECOND 2-SECONDS OF DATA.  
SUNSPOT, 28 MARCH, 1980, 1130 HRS. LOCAL TIME.  
COMPENSATED APERTURE 30 CM DIAMETER.

POWER NCHAN = 11

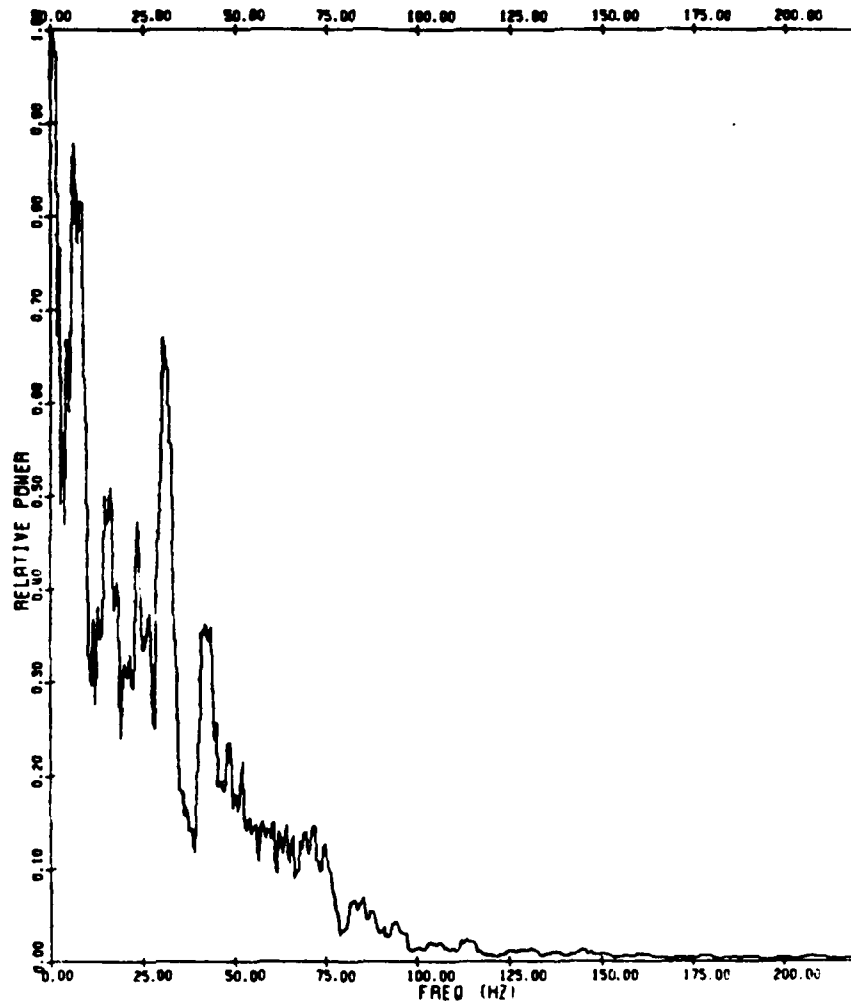


Figure 10 - Power Spectrum of Actuator Drive Signal

TABLE 4

## DATA ANALYSIS SUMMARY

## Temporal Bandwidth and Drive Distances

A. TILT

Date and Time	Conditions	Tape #	Bandwidth		Aper- ture Meters	Drive Angle or Distance
			Cutoff	10%		
5/28/80 1130	SUNSPOT 58°	3A	X	50	31	0.3
			Y	60	31	
4/06/80 0230	ARCTURUS 70°	8	X	100	40	+ 1.78 arc sec RMS
			Y	55	20	+ 0.87 arc sec RMS
4/06/80 2000	SIRIUS 30°	9A	X	35	12	+ 2.16 arc sec RMS
			Y	18	8	+ 1.71 arc sec RMS

B. MPM

3/28/80 1130	SUNSPOT 58°	3A		168	124	0.3
			2	123	62	
3/31/80 2120	SIRIUS 20°	6A		120	50	+ 0.48 μM RMS
4/06/80 2000	SIRIUS 30°	9A		125	55	0.46
3/31/80 2130	SIRIUS 18°	6B		100	50	+ 0.48 μM RMS
3/31/80 2140	SIRIUS 17°	6C		100	45	+ 0.70 μM RMS
3/31/80 2150	SIRIUS 16°	6D		90	20	+ 0.50 μM RMS

C. INTENSITY

4/06/80 2000	SIRIUS	9A		104	34	
-----------------	--------	----	--	-----	----	--

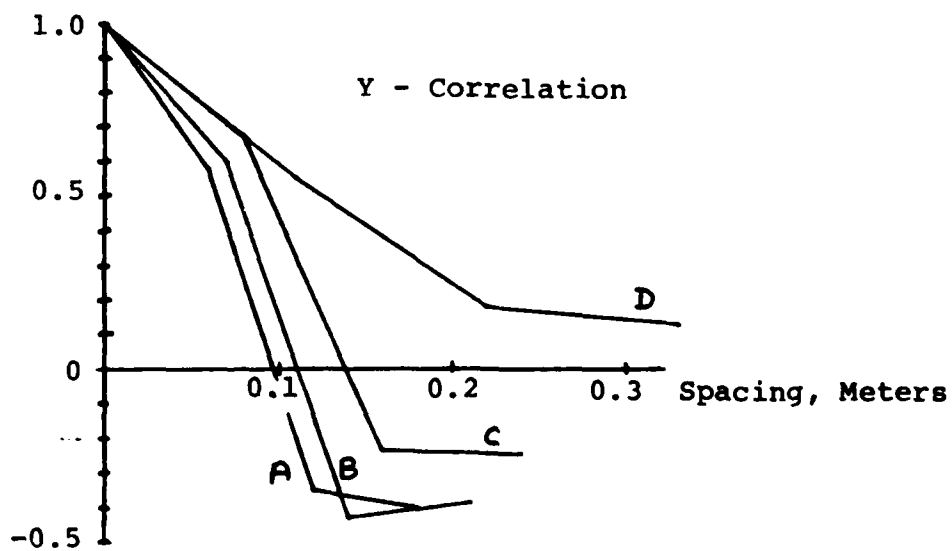
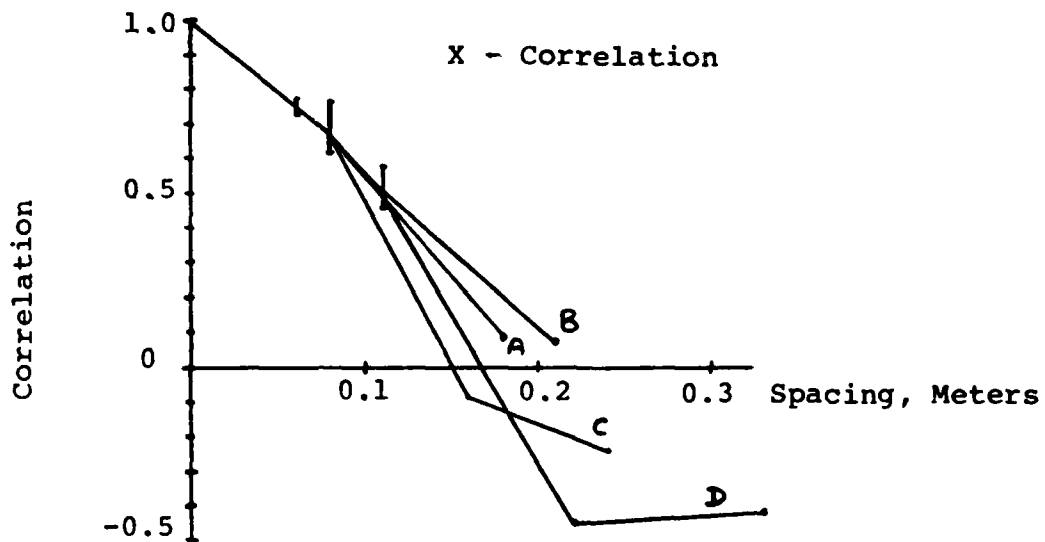


Fig. 11 Spatial Correlation, Night Observations from Tape No. 6, Sirius, 31 March 1980. Each point is a 2-second average.

A = 20° Elevation      B = 18° Elevation  
 C = 17° Elevation      D = 16° Elevation

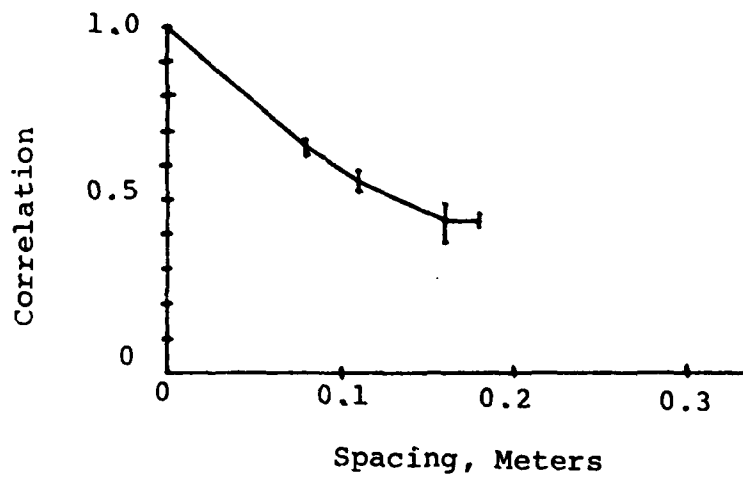


Fig. 12 Intensity Correlation, Night Observations,  
from Tape No. 9A, Sirius, 6 April 1980.  
Each point is a 2-second average.  
Elevation angle  $30^{\circ}$ .

The spatial correlation of the MPM drive signals is shown in Figure 11, for night-time operation using 2-second samples, taken over a 30 minute period. The distance for 50% correlation varies between 5 and 15 cm. Random changes between samples appear to dominate any systematic change with elevation or time. Spatial correlation of the photometric intensity of the received wavefront is shown in Figure 12. The 50% correlation distance was between 11 and 15 cm, somewhat greater than that for the wavefront phase.

#### 4. ANALYSIS

The optical effects of atmospheric turbulence can be characterized by three parameters: the spatial coherence length,  $r_0$ ; the isoplanatic angle  $\theta_0$ ; and the temporal bandwidth  $f_0$ . The temporal bandwidth is mainly determined by wind velocities and is normally in the order of a few hundred Hertz. To keep the compensation error due to temporal bandwidth small, the wavefront measurement time and the servo response time must not exceed a few milliseconds. With a bright object such as the sun, this presents no problem because the large photon flux allows the wavefront measurement to be made with a high signal to noise ratio using an integration time of less than a millisecond. Also, the response of current deformable mirrors is well above 1 KHz. The atmospheric bandwidth,  $f_0$ , is therefore not a practical limitation, so we will concentrate attention on the remaining two parameters.

##### 4.1 Coherence Length

The usually accepted definition of the turbulence coherence length,  $r_0$ , due to Fried, is in the form of the turbulence structure function,

$$\langle (\theta_1 - \theta_2)^2 \rangle = D(r) = 6.88 \left(\frac{r}{r_0}\right)^{5/3} \text{ radians}^2$$

which defines the mean square phase variance between two points on the wavefront separated by distance  $r$ . The mean square phase variance is a measure of the total integrated turbulence of the atmosphere along one line of sight. Due to the exponential fall-off of turbulence strength with altitude, the lower layers of the atmosphere have a dominant effect on  $r_0$ . Because of solar heating near the ground, a strong diurnal effect is present. This effect is shown in Figure 13 which is derived from data obtained by Walters et al. at White Sands (Reference 2). Note that relatively high values of  $r_0$  (low turbulence) occur during the two periods of temperature equilibrium around sunrise and sunset.

In addition to the diurnal variation, the effective value of  $r_0$ , normally specified at zenith, is a function of zenith angle,  $\zeta$ :

$$r_0(\zeta) = r_0 \cos^{3/5} \zeta$$

at low elevations, therefore, the effective value of  $r_0$  may be very small (high turbulence) even though the zenith seeing may be good.

To determine the effective solar seeing, we must therefore include both diurnal and zenith angle effects, as shown in Figure 14. The best periods of seeing occur in early morning and late afternoon, but it should be noted that the values of  $r_0$  obtained (5 to 6 cm) even then are only half of those encountered at night at good astronomical sites.

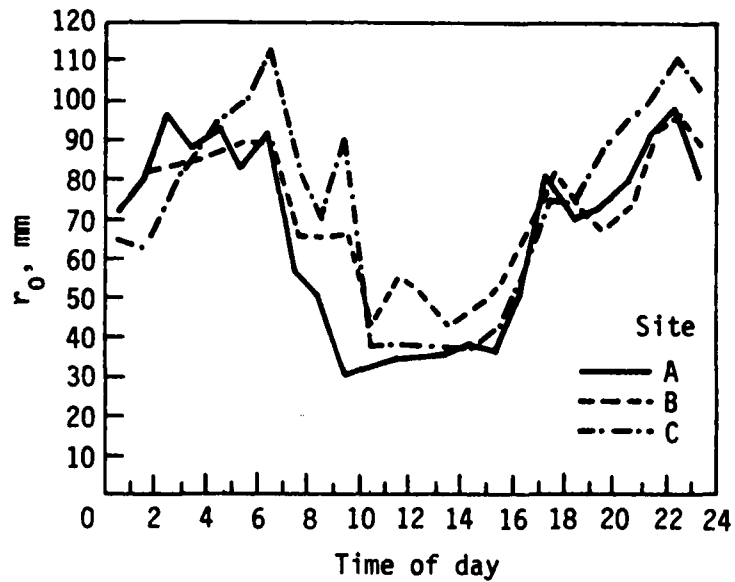


Fig. 13 Diurnal variation of turbulence coherence length at sites A, B, and C

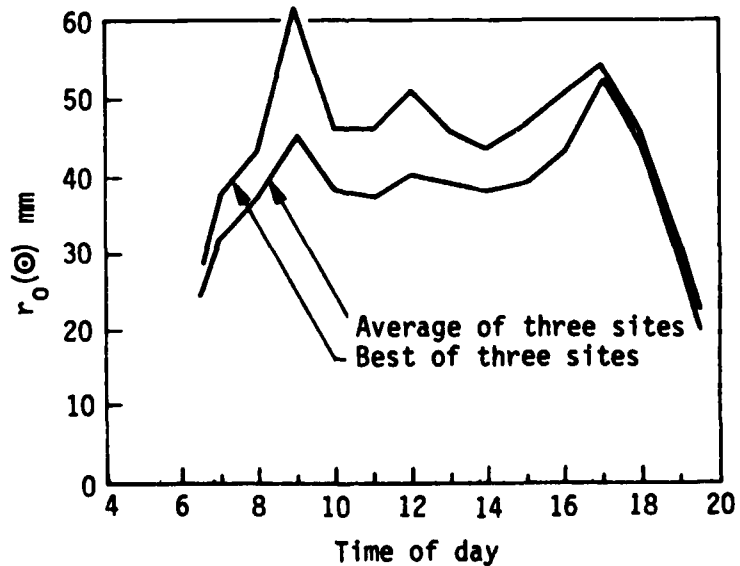


Fig. 14 Variation of effective solar coherence length

The practical importance of the coherence length  $r_0$  to a wavefront compensation system is that it determines the wavefront fitting error, which is given by:

$$\sigma_F^2 = K \left( \frac{d}{r_0} \right)^{5/3}$$

where  $d$  = spacing of deformable mirror actuators

$K$  = fitting coefficient of mirror

The factor  $K$  depends on the shape or influence function of the actuators; for Itek's monolithic piezoelectric mirror it has the value of 0.01 waves. The value of  $\sigma_F$  can always be reduced by decreasing  $d$ . In practical systems, the number of actuators is fixed and  $d$  can only be reduced by using a smaller aperture. However, this limits the angular resolving power of the telescope, so a compromise is necessary. For the experiments described in Section 3, an optical zoom system was used between the telescope and the RTAC to vary the effective aperture between 30 cm and 60 cm, corresponding to values of  $d$  between 6 cm and 12 cm, in order to match the expected range of  $r_0$ .

#### 4.2 Isoplanatic Patch

If we consider a layer of turbulence with a specific coherence length, then it is obvious that the isoplanatic angle over which the wavefront is correlated will be largest when the layer is near the telescope aperture and smallest when it is far from the aperture. The isoplanatic angle,  $\theta_0$  is therefore determined by the vertical distribution, or profile, of atmospheric turbulence, with the higher layers having the dominant effect. The isoplanatic angle is largely independent of  $r_0$ , and may be relatively independent of diurnal effects. The isoplanatic angle  $\theta_0$  can be defined in a similar way to coherence length:

$$D(\theta) = 6.88 \left( \frac{\theta}{\theta_0} \right)^{5/3} \text{ radians}^2$$

which defines the mean square phase variance between two rays at an angle  $\theta$ . Measurements made by various workers (References 3 and 4) suggest that the value of  $\theta_0$  as defined above is generally in the region of 3 to 6 arc seconds, measured at the zenith.

The isoplanatic angle is strongly dependent on zenith angle, the relation being:

$$\theta_0(z) = \theta_0 \cos^{8/5} z$$

The isoplanatic angle  $\theta_0$  defined above is a property of the atmospheric turbulence profile, independent of any compensation system and pertains to single rays traversing the atmosphere.

When a point source is used for wavefront sensing, the measured wavefront is exactly correct in the direction of the reference source. A wavefront error variance proportional to  $\theta^{5/3}$  is incurred as the field angle  $\theta$  increases.

With an extended object such as the sun, a complication arises in that a finite area of the object, encompassing some surface detail such as granulation, must be used as the reference source. The wavefront is then compensated with regard to the average error over this finite reference area. It is therefore of interest to determine the effect of the size of this reference area on the anisoplanatic error of the compensated image.

The results of an analysis made at Itek are summarized in Figure 15 which shows the mean square wavefront error  $\sigma_2^2$  due to anisoplanatism, normalized by the function  $6.88 (\theta_F/\theta_0)^{5/3}$ , as a function of  $\theta/\theta_F$ , where  $\theta$  is the field angle and  $\theta_F$  is the radius of the area used for wavefront reference. The main effect of using a finite area rather than a point source for wavefront reference is to increase the wavefront error in the center of the field-of-view and to reduce it at the edge of the field.

It should be noted that this effect is a property of the atmosphere and is present even with a "perfect" wavefront sensor. Also, the minimum size of the wavefront reference field is determined by the scale of the solar detail (such as the granulation pattern); it is not a discretionary variable and is the same for any type of wavefront sensor.

To determine the overall image resolution as a function of field angle, both anisoplanatic and fitting error effects must be taken into account. Figure 16 shows plots of on-axis image intensity versus field angle for typical conditions when viewing the sun near the zenith and at 30 degrees elevation. At the zenith, good compensation is obtainable over a field of about 2 arcseconds in diameter. At 30 degrees elevation however, the isoplanatic angle has shrunk to one third of its zenith value and  $r_0$  to two thirds of its zenith value, resulting in a drastically reduced compensation patch less than 1 arcsecond in diameter.

It is of interest to determine how the size of the compensated solar image varies during the day. The compensated image size is defined arbitrarily as the radius at which the wavefront error is 0.20 waves rms, giving an on-axis image intensity of 0.2 of its unaberrated value. Using the diurnal variation of  $r_0$  from Figure 14 the results shown in Figure 17 are obtained.

These results show that with solar image compensation, the largest compensated area is obtained around midday. During the periods of good uncompensated seeing in early morning and late afternoon, the size of the compensated patch is too small to be useful.

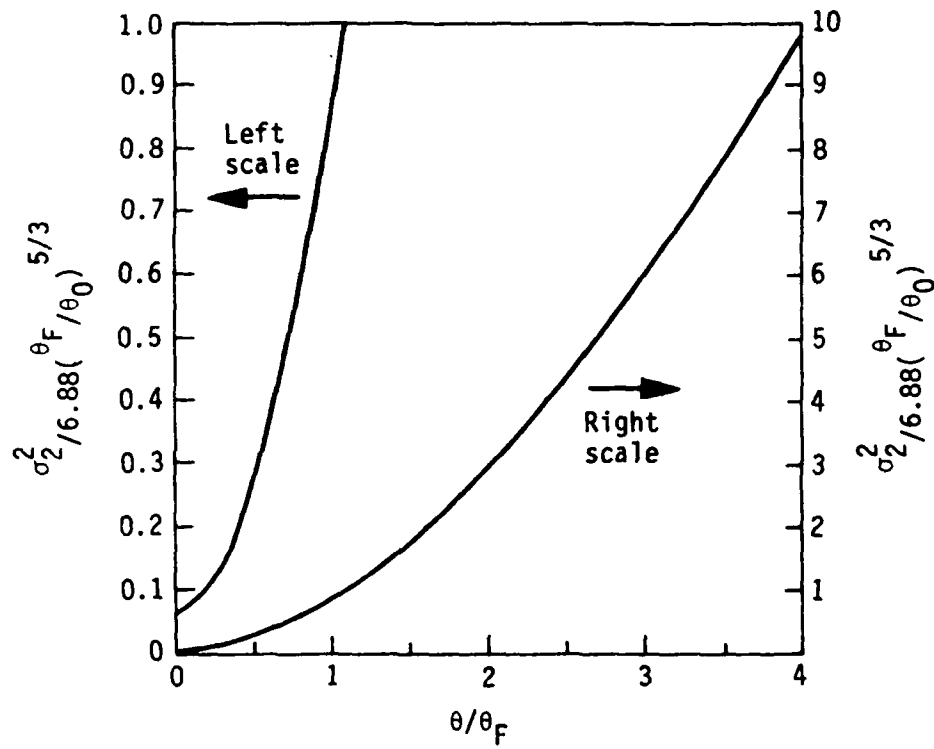


Fig. 15 Wavefront error due to anisoplanatism

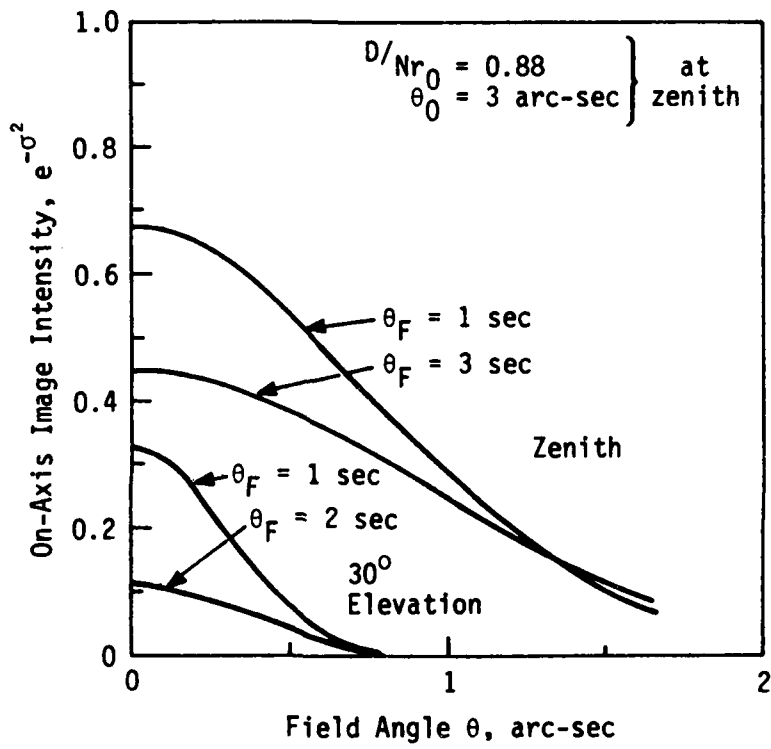


Fig. 16 Image quality versus field angle

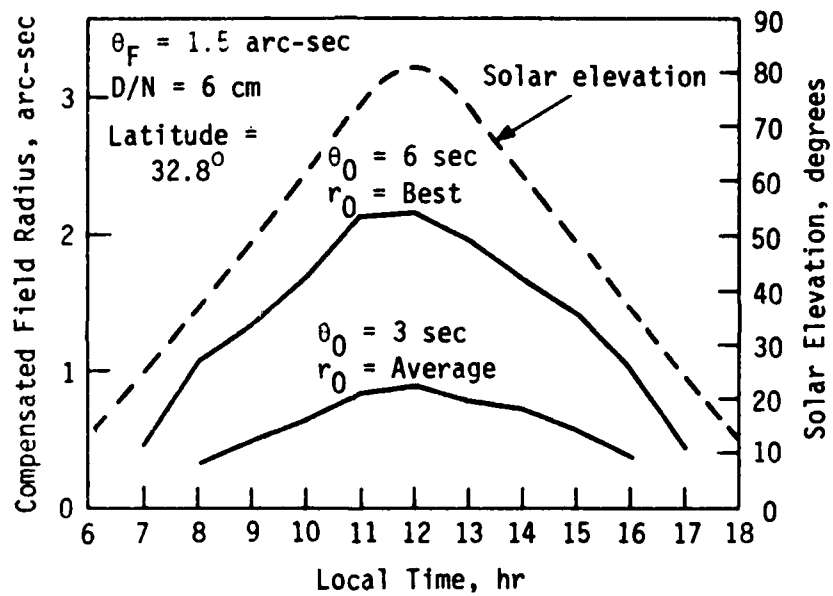


Fig. 17 Diurnal variation of solar compensated field for 0.2-wave rms error

Note:  $r_0$  values refer to Figure 14.

This analysis provides an insight into the results obtained during the solar image compensation experiment, as discussed in the following section.

## 5. CONCLUSIONS

When observing stars, the real-time compensation system operated as expected, sharpening the image and producing a significant increase in the peak intensity. The quality of the compensated image was generally consistent with the fitting error limitations due to the relation of actuator spacing,  $d$  to atmospheric  $r_0$ , as described in Section 4.1. Observations of double stars were somewhat restricted due to magnitude limitations. The data obtained indicate that the isoplanatic patch radius at night was between 2 and 4 arc seconds measured near the zenith.

The results obtained when observing the sun were not as expected. On most occasions the RTAC appeared to operate normally; the active mirror feedback loops were converged and stable; the indicated residual error was reduced to a small value; the real-time data outputs from the RTAC (such as the MPM drive signals shown in Figure 9) were exactly as expected in terms of drive distance and power spectrum. However, a significant increase in image resolution was obtained only on rare and unpredictable occasions.

While initially these results were puzzling, we believe that they can be explained in terms of the system parameters, particularly the values of  $r_0$  and  $\theta_0$  in relation to the aperture size and number of actuators on the RTAC.

Figure 17 shows that under average conditions ( $r_0 = 4$  cm,  $\theta_0 = 3$  arc seconds) with an actuator spacing of 6 cm and a wavefront sensor field stop radius of 1.5 arc seconds, the compensated image radius (for 0.2 waves rms error) is less than 1 arc second. During the periods of good solar seeing around 8 to 9 AM, the compensated image radius is less than 0.5 arc seconds.

With a 21-element active mirror having 5 actuators across the diameter, the 6 cm actuator spacing corresponds to a compensated telescope aperture of 30 cm; the classic resolving power of this aperture at  $\lambda = 500$  nm is 0.4 arc seconds. The number of resolution elements across the diameter of the compensated field is therefore between 2.5 and 5. Such a small compensated area is difficult to distinguish visually in a video image frame covering 15 arc seconds, especially when the image is of low contrast.

On the occasions when a noticeable improvement in image quality was obtained (Figure 5, for example), the area of improvement was relatively large (about 6 arc seconds in this case) indicating that on this particular occasion  $\theta_0$  was much larger than its average value.

The results of the experiment are generally confirmed by the analysis, which shows that even with a perfectly functioning real-time compensation system, the size of the compensated area on the sun is determined primarily by atmospheric conditions and is normally only one or two arc seconds in diameter.

The benefits of real-time compensation become more apparent as the telescope aperture is increased, because a larger number of image elements can then be resolved within this compensated area.

#### REFERENCES

1. J. W. Hardy, J. E. Lefebvre and C. L. Koliopoulos, "Real-Time Atmospheric Compensation", J.Opt.Soc.Am., Vol. 67, pp 360-369, 1977.
2. D. L. Walters, D. L. Favier and J. R. Hines, "Vertical Path Atmospheric MTF Measurements", J.Opt. Soc.Am., Vol. 69, pp 828-837, 1979.
3. R. Barletti, G. Ceppatelli, L. Paterno, A. Righini and N. Speroni, "Mean Vertical Profile of Atmospheric Turbulence Relevant for Astronomical Seeing", J.Opt. Soc.Am., Vol 66, pp 1380-1383, 1976.
4. M. G. Miller and P. L. Zieske, "Turbulent Environment Characterization", Final Technical Report, June 1979, RADC-TR-79-131.

DATE  
FILMED  
— 8